

# Journal of Materials Chemistry A

Materials for energy and sustainability

Accepted Manuscript

This article can be cited before page numbers have been issued, to do this please use: J. Li, W. Tian, S. Du, L. Wang, H. Zhang, Q. Chen, C. Zhou, L. Shang, G. Chen, T. Zhang and X. Meng, *J. Mater. Chem. A*, 2025, DOI: 10.1039/D5TA05338B.



This is an Accepted Manuscript, which has been through the Royal Society of Chemistry peer review process and has been accepted for publication.

Accepted Manuscripts are published online shortly after acceptance, before technical editing, formatting and proof reading. Using this free service, authors can make their results available to the community, in citable form, before we publish the edited article. We will replace this Accepted Manuscript with the edited and formatted Advance Article as soon as it is available.

You can find more information about Accepted Manuscripts in the [Information for Authors](#).

Please note that technical editing may introduce minor changes to the text and/or graphics, which may alter content. The journal's standard [Terms & Conditions](#) and the [Ethical guidelines](#) still apply. In no event shall the Royal Society of Chemistry be held responsible for any errors or omissions in this Accepted Manuscript or any consequences arising from the use of any information it contains.

## PAPER

**Anthraquinone-modified triazine rich g-C<sub>3</sub>N<sub>4</sub> for high efficiency photocatalytic H<sub>2</sub>O<sub>2</sub> synthesis *via* promoting singlet oxygen conversion<sup>†</sup>**Received 00th January 20xx,  
Accepted 00th January 20xx

DOI: 10.1039/x0xx00000x

Junlin Li<sup>ab</sup>, Wenyu Tian<sup>a</sup>, Shihao Du<sup>b</sup>, Lingsong Wang<sup>b</sup>, Hanxu Zhang<sup>b</sup>, Qirong Chen<sup>c</sup>, Chao Zhou<sup>\*b</sup>, Lu Shang<sup>b</sup>, Guangbo Chen<sup>\*b</sup>, Tierui Zhang<sup>b</sup>, Xiangfu Meng<sup>\*a</sup>

Photocatalytic hydrogen peroxide (H<sub>2</sub>O<sub>2</sub>) production *via* two-electron oxygen reduction reaction (2e<sup>-</sup> ORR) represents a sustainable alternative to the energy-intensive anthraquinone (AQ) process. Although graphitic carbon nitride (g-C<sub>3</sub>N<sub>4</sub>) demonstrates significant advantages in photocatalytic H<sub>2</sub>O<sub>2</sub> synthesis, its efficiency is severely limited by rapid charge recombination and the competitive oxidation of the critical superoxide radical (·O<sub>2</sub><sup>-</sup>) intermediate to singlet oxygen (<sup>1</sup>O<sub>2</sub>). Herein, AQ-modified triazine rich g-C<sub>3</sub>N<sub>4</sub> (AQ/CN-x%) was successfully constructed through molten salt-assisted polycondensation and amidation grafting reactions. The coexistence of triazine and heptazine units not only promotes the separation of photogenerated charges but also provides more modification sites for AQ anchoring. Due to its strong electron-withdrawing nature, the AQ modification further enhances the separation of photogenerated charge carriers. More importantly, the AQ moiety effectively converts the competitively generated <sup>1</sup>O<sub>2</sub> into H<sub>2</sub>O<sub>2</sub> *via* hydroanthraquinone intermediates, significantly improving the photocatalytic H<sub>2</sub>O<sub>2</sub> synthesis efficiency in pure water. The optimized AQ/CN-70% catalyst achieved a remarkable H<sub>2</sub>O<sub>2</sub> production rate of 165.3 μmol·g<sup>-1</sup>·h<sup>-1</sup>, representing 4.6-fold and 13.8-fold enhancements over CN-70% and g-C<sub>3</sub>N<sub>4</sub>, respectively. This work provides a novel strategy for converting <sup>1</sup>O<sub>2</sub> into H<sub>2</sub>O<sub>2</sub> by incorporating strongly electron-withdrawing AQ units into the triazine rich g-C<sub>3</sub>N<sub>4</sub> framework, leading to a significant enhancement in photocatalytic H<sub>2</sub>O<sub>2</sub> synthesis activity.

**Introduction**

As a high-value multifunctional reagent, hydrogen peroxide (H<sub>2</sub>O<sub>2</sub>) is extensively employed in wastewater treatment, medical disinfection, and industrial bleaching.<sup>1</sup> Contemporary industrial H<sub>2</sub>O<sub>2</sub> manufacturing predominantly employs the anthraquinone (AQ) process, which is mainly derived by significant drawbacks, including reliance on precious-metal catalysts, substantial organic waste generation, and high energy consumption.<sup>2</sup> Photocatalytic H<sub>2</sub>O<sub>2</sub> synthesis from H<sub>2</sub>O/O<sub>2</sub> and solar energy has emerged as a promising sustainable alternative.<sup>3</sup> Designing and preparing efficient and stable

photocatalysts is one of the key technologies to promote the photocatalytic synthesis of H<sub>2</sub>O<sub>2</sub>. To date, inorganic semiconductors, metal-organic frameworks (MOF), covalent organic frameworks (COF) and conjugated polymers have been explored as photocatalysts to produce H<sub>2</sub>O<sub>2</sub>.<sup>4-7</sup> Among these photocatalysts, graphitic carbon nitride (g-C<sub>3</sub>N<sub>4</sub>) is considered practically promising for photocatalytic H<sub>2</sub>O<sub>2</sub> production due to its stable physicochemical properties, easy of modification and low-cost synthesis. However, the photocatalytic efficiency for H<sub>2</sub>O<sub>2</sub> generation from H<sub>2</sub>O and O<sub>2</sub> remains limited due to the rapid recombination of photogenerated charge carrier and the strong completion from singlet oxygen (<sup>1</sup>O<sub>2</sub>) generation.<sup>8</sup> Unfortunately, little attention has been paid to the utilization and transformation of <sup>1</sup>O<sub>2</sub> during the photocatalytic synthesis of H<sub>2</sub>O<sub>2</sub>.<sup>9,10</sup>

In photocatalytic process, <sup>1</sup>O<sub>2</sub> is usually generated through two pathways: (1) energy transfer from excited dye molecules to the triplet ground state of O<sub>2</sub> or (2) oxidation of superoxide radicals (·O<sub>2</sub><sup>-</sup>) by photogenerated holes. These competing pathways inevitably lead to energy loss and depletion of critical intermediates, thereby reducing the efficiency of photocatalytic H<sub>2</sub>O<sub>2</sub> production. Recently, it has been reported that <sup>1</sup>O<sub>2</sub> played

<sup>a</sup> Department of Chemistry, Capital Normal University, Beijing 100048, China.<sup>b</sup> Key Laboratory of Photochemical Conversion and Optoelectronic Materials, Technical Institute of Physics and Chemistry, Chinese Academy of Sciences, Beijing, 100190, China.<sup>c</sup> Institute of Analysis and Testing, Beijing Academy of Science and Technology (Beijing Center for Physical and Chemical Analysis), Beijing, 100094, China<sup>†</sup> Electronic Supplementary Information (ESI) available. See

DOI: 10.1039/x0xx00000x

\* Corresponding authors: czhou@mail.ipc.ac.cn (C. Zhou), gchen@mail.ipc.ac.cn (G. Chen), xfmeng@cnu.edu.cn (X. Meng).



## PAPER

a crucial role in promoting photocatalytic  $\text{H}_2\text{O}_2$  generation. For instance, the unique resonance energy transfer process from the strong excitonic effect of g- $\text{C}_3\text{N}_4$  can effectively active  $\text{O}_2$  to generate high-energy  $^1\text{O}_2$ .<sup>11</sup> Thus, an efficient  $^1\text{O}_2$ -engaged one-step two-electron pathway simplified the reaction procedure and optimized the intermediate energy levels, which improved the production activity of  $\text{H}_2\text{O}_2$  by 12.2 times.<sup>12</sup> Through an excitation energy and electron transfer, dioxygen molecule can be converted to a highly active singlet oxygen intermediate and then is reduced to  $\text{H}_2\text{O}_2$  *via* the photogenerated electrons with a reduced barrier.<sup>13,14</sup> However, the pronounced exciton effect in  $\text{C}_3\text{N}_4$  usually conflicts with charge carrier separation and transfer.<sup>15</sup> Recently, a [4+2] cycloaddition reaction was proposed to convert  $^1\text{O}_2$  into  $\text{H}_2\text{O}_2$ . The generation of  $^1\text{O}_2$  through the oxidation of superoxide radical ( $\cdot\text{O}_2^-$ ), followed by its conversion into endoperoxides *via* [4+2] cycloaddition, facilitates the charge separation and enhances the selectivity of  $\text{O}_2$  reduction to  $\text{H}_2\text{O}_2$ .<sup>16</sup> From the perspective of energy efficiency optimization, developing a strategy that can not only promote the separation of photo-generated charges but also rapidly convert  $^1\text{O}_2$  into  $\text{H}_2\text{O}_2$  holds great promise for enhancing the efficiency of  $\text{H}_2\text{O}_2$  photosynthesis.

Herein, AQ-modified triazine rich g- $\text{C}_3\text{N}_4$  (AQ/CN-x%) was synthesized *via* molten salt assisted polycondensation and subsequent amidation grafting reaction.<sup>17,18</sup> The effect of AQ units in photocatalytic  $\text{H}_2\text{O}_2$  production was systematically investigated. Combined experimental and theoretical analyses demonstrate that AQ units, acting as electron acceptors, substantially enhance charge separation efficiency. More importantly, the AQ/ $\text{H}_2\text{AQ}$  redox cycle effectively facilitates the conversion of  $\text{O}_2$  into  $\text{H}_2\text{O}_2$ .<sup>18</sup> This suggests that AQ may also mediate the photocatalytic transformation of  $^1\text{O}_2$  to  $\text{H}_2\text{O}_2$ , revealing a previously overlooked catalytic capability. The optimized AQ/CN-70% exhibited a  $\text{H}_2\text{O}_2$  production rate of 165.3  $\mu\text{mol}\cdot\text{g}^{-1}\cdot\text{h}^{-1}$  under ambient atmospheric condition, representing 13.8-fold increase over pristine g- $\text{C}_3\text{N}_4$ . This work presents an innovative design strategy involving AQ functionalization of carbon nitride to simultaneously improve charge separation efficiency and promote the conversion of  $^1\text{O}_2$  to  $\text{H}_2\text{O}_2$ , thereby boosting the overall efficiency of  $\text{H}_2\text{O}_2$  photosynthesis.

## Experimental

### Materials

Melamine (99%), acetonitrile (99.9%), anthraquinone-2-carboxylic acid (AQ-COOH, 98%), Silver nitrate ( $\text{AgNO}_3$ , 99.8%) and p-Benzoquinone (BQ, 99%) were purchased from Sigma-Aldrich. Potassium chloride (KCl, 99.5%) was obtained from Alfa Aesar. Lithium chloride (LiCl, 99.8%), Potassium biphthalate (PT, 99.9%), Potassium Iodide (KI, 99%) and  $\beta$ -Carotene (96%) were received from Innochem. There was no further purification treatment on all of the chemicals.

### Synthesis of CN-x% and BCN

1.0 g of melamine was ground with 10 g of KCl/LiCl mixed molten salts (with KCl mass fraction x%) for 30 min. The resulting mixture was then transferred to a muffle furnace and calcinated at 550 °C for

4 h at a heating rate of 5 °C $\cdot\text{min}^{-1}$ . After cooling to ambient temperature, the crude product was repeatedly washed with deionized water, isolated by centrifugation, and dried at 60 °C overnight to obtain the CN-x% composite. For example, CN-70% was synthesized using 7.0 g of KCl, 3.0 g of LiCl and 1.0 g of melamine. For comparison, bulk g- $\text{C}_3\text{N}_4$  (BCN) was also prepared using the same procedure, but without the addition of molten salts.

### Synthesis of AQ/CN-x%

A total of 0.4 g of CN-x% was dispersed in 40 mL of acetonitrile, followed by the addition of 0.1 g of anthraquinone-2-carboxylic acid (AQ-COOH). The mixture was sonicated for 30 min to ensure uniform dispersion and then stirred at 50 °C for 12 h. After cooling to room temperature, the product was collected by filtration, thoroughly washed with deionized water and ethanol to remove unreacted species, centrifuged, and vacuum-dried at 60 °C overnight to obtain AQ/CN-x% composite. For comparison, AQ/BCN was synthesized *via* the similar method with BCN as the substrate.

### Characterizations

X-ray diffraction (XRD) patterns were acquired on a Bruker D8 Advance X diffractometer using Cu K $\alpha$  radiation ( $\lambda = 1.5405 \text{ \AA}$ ) at 40 kV. Scanning electron microscopy (SEM) was performed on a Hitachi S-4800 microscope. Transmission electron microscopy (TEM) and high-angle annular dark-field scanning TEM (HAADF-STEM) with energy-dispersive X-ray spectroscopy (EDX) mapping were conducted using Hitachi HT-7700 (100 kV) and JEOL JEM-ARM300F (300 kV) instruments, respectively. X-ray photoelectron spectroscopy (XPS) was carried out on an ESCALAB 250Xi spectrometer with Al-K $\alpha$  excitation, and all binding energies were calibrated to the carbon C 1s peak at 284.8 eV. The  $^{13}\text{C}$  solid-state nuclear magnetic resonance (NMR) spectra were recorded on Bruker Ascend TM 400WB. UV-Vis diffuse reflectance spectra were obtained using an Agilent Cary 7000 spectrophotometer equipped with an integrating sphere. Fourier transform infrared (FTIR) spectra were recorded using a Varian Excalibur spectrometer. Specific surface areas were determined by Brunauer-Emmett-Teller (BET) analysis on a Quadrasorb SI-MP porosity analyzer. The steady-state photoluminescence spectra (PL) and time-resolved photoluminescence spectra (TRPL) were measured at room temperature using time-correlated single-photon counting (Edinburgh Instruments, FLS1000). Femtosecond transient absorption spectroscopy (fs-TAS) measurements were performed employing a Coherent Vitara-Legend Elite-Helios system. For fs-TAS, aqueous catalyst dispersions (0.5  $\text{mg}\cdot\text{mL}^{-1}$ ) were sonicated for 30 min prior to measurement in a microcuvette at room temperature, using 320 nm excitation with probe wavelengths ranging from 320 to 800 nm. Electron paramagnetic resonance (EPR) measurement was conducted on an E500 spectrometer.

### Photocatalytic activity evaluation

For photocatalytic testing, 20 mg of catalyst was dispersed in 20 mL of deionized water and sonicated for 30 min to ensure uniform dispersion. The photocatalytic reactions were conducted under



visible light irradiation ( $\lambda \geq 420$  nm) using a 300 W Xenon lamp equipped with a 420 nm cut-off filter, in an open quartz tube under atmospheric conditions, with air serving as the  $O_2$  source. Reaction aliquots (1 mL) were collected at 60-min intervals, centrifuged, and filtered through a 0.22  $\mu$ m polyethersulfone (PES) membrane. The  $H_2O_2$  concentration was determined by iodometry: 500  $\mu$ L of 0.1 M PT solution and 500  $\mu$ L of 0.4 M KI solution were sequentially added to 1 mL of the filtrate. After reaction in the dark for 1 h, the absorbance at 350 nm was measured using a UV-vis spectrophotometer. The  $H_2O_2$  concentration was calculated from a pre-established calibration curve.

### Computational details

To obtain a reasonable initial geometry for the catalyst model, we first conducted a conformational search using CREST 3.0.1<sup>19</sup> with the GFN2-xTB<sup>20</sup> tight-binding quantum chemical method. The lowest-energy conformer was then selected for further density functional theory (DFT) calculations. Geometry optimization was performed at the (u)B3LYP/def2SVP level,<sup>21–26</sup> employing Becke's three-parameter hybrid functional combined with the Lee-Yang-Parr correlation functional. To accurately account for long-range dispersion interactions, Grimme's D3<sup>27</sup> dispersion correction with Becke-Johnson (BJ)<sup>28</sup> damping was applied. Frequency calculations were conducted at the same level to confirm that a true minimum (i.e., no imaginary frequencies) had been obtained on the potential energy surface. Time-dependent density functional theory (TD-DFT) calculations were performed at TD-B3LYP-GD3(BJ)/def2SVP level of theory and the hole-electron analysis was based on these calculations using Multiwfn 3.8(dev).<sup>29</sup> All calculations were done using GAUSSIAN 16 C.01.

## Result and discussion

### Structure and composition

The synthesis route of AQ/CN-x% is illustrated in Fig. 1a. CN-x% (where x denotes the mass fraction of KCl in the molten salts) containing both triazine and heptazine units was first prepared *via* molten salt-assisted thermal condensation. Subsequently, AQ units were introduced through an amidation reaction.<sup>18</sup> As revealed by SEM and TEM images (Fig. 1b, Figs. S1a,b, and Figs. S2a-c), both CN-70% and AQ/CN-70% exhibit a hierarchical structure of nanorod structure, with individual rods approximately 50 nm in diameter assembled into larger architectures. Compared to direct calcination, molten salt-assisted thermal condensation is more effective in promoting the reconstruction of carbon nitride crystals and the transformation of their aggregated states. HAADF-STEM and corresponding EDS mapping images (Fig. 1c, d) visually demonstrate the spatial distribution of C and N elements, along with trace amounts of K and Cl, within AQ/CN-70%. HRTEM images (Fig. 1e-g) further confirm the coexistence of triazine and heptazine units in the hierarchical structure of AQ/CN-70%. Fourier-filtered analysis of selected regions resolved distinguishable lattice fringes with characteristic d-spacings of 0.34 and 0.32 nm, corresponding to the (002) crystallographic planes of triazine and heptazine units, respectively.<sup>30</sup>

XRD analysis further confirmed the crystalline phase composition of the catalysts. As depicted in Fig. 1h, BCN only showed characteristic peaks at 13.0° and 27.5° corresponding to the (100) and (002) planes of g-C<sub>3</sub>N<sub>4</sub>, respectively. In contrast, CN-70% displayed distinct diffraction peaks characteristic of both triazine and heptazine units. Peaks at 12.0°, 20.9°, 24.2°, 29.1°, and 32.3° were assigned to the (100), (110), (200), (102), and (210) planes of the triazine structure (TCN), respectively, while the peak at 28.1° was attributed to the (002) plane of the heptazine unit (HCN).<sup>30</sup> Notably, AQ functionalization did not alter the crystalline phase composition of CN-70%. Moreover, the triazine/heptazine ratio could be tuned by adjusting the KCl content in the molten salts (Fig. S3). As KCl content decreased, the intensity of triazine-related peaks increased, indicating that KCl was more beneficial to inducing heptazine unit formation, which was consistent with previous literature reports.<sup>32</sup>

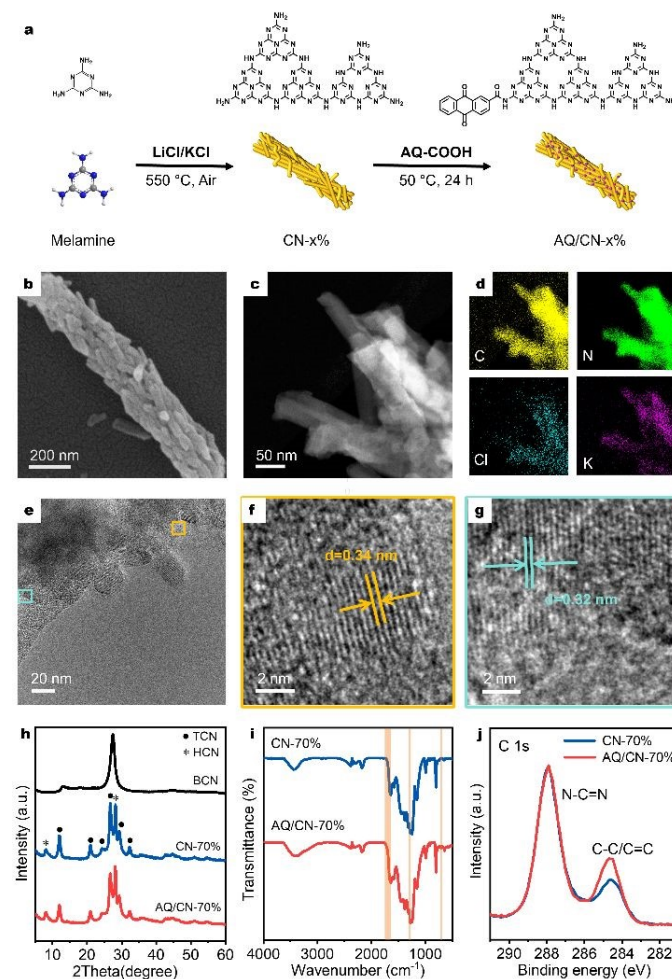


**Fig. 1** (a) Schematic illustration of the synthesis route for AQ/CN-x%, (b) SEM image of AQ/CN-70%, (c, d) HAADF-STEM and related EDS elemental mapping images of AQ/CN-70%, (e-g) TEM and HRTEM of AQ/CN-70%, with lattice fringes from regions marked by coloured boxes in Fig. 1e, (h) XRD patterns of BCN, CN-70%, and AQ/CN-70%, (i) FTIR spectra of CN-70% and AQ/CN-70%, (j) XPS spectra of C 1s for CN-70% and AQ/CN-70%.

To confirm the successful AQ modification of CN-70%, FTIR and XPS were carried out. Compared with CN-70%, a new peak appeared at 698 cm<sup>-1</sup> in AQ/CN-70% (Fig. 1i), corresponding to the bending





## PAPER

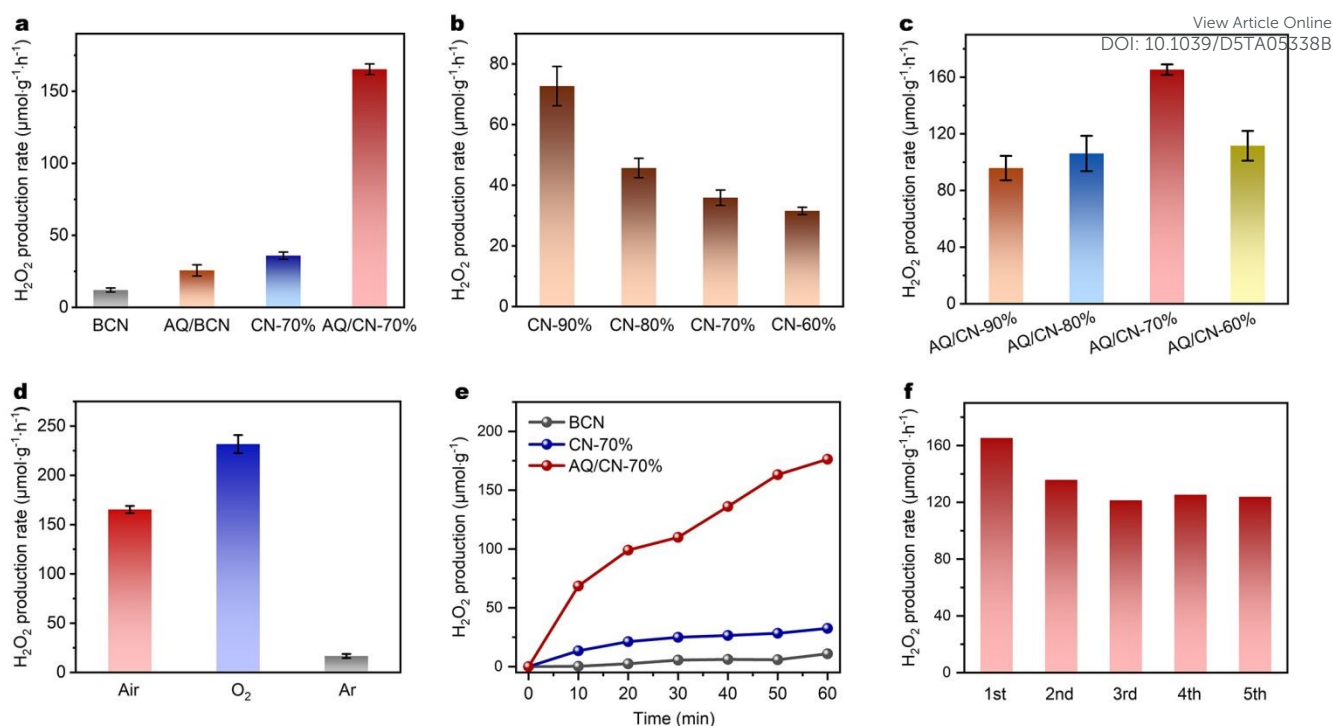


**Fig. 2** (a) Photocatalytic H<sub>2</sub>O<sub>2</sub> production rates of BCN, AQ/BCN, CN-70% and AQ/CN-70%, (b, c) H<sub>2</sub>O<sub>2</sub> production rates of CN-*x*% and AQ/CN-*x*%, (d) Photocatalytic H<sub>2</sub>O<sub>2</sub> production rate of AQ/CN-70% under varying atmospheres, (e) Time-dependent H<sub>2</sub>O<sub>2</sub> production kinetics of BCN, CN-70% and AQ/CN-70%, (f) Photocatalytic cyclic-stability of AQ/CN-70% for H<sub>2</sub>O<sub>2</sub> production. Reaction conditions: 300 W Xenon light source equipped with a cut-off filter ( $\lambda \geq 420$  nm); irradiation intensity: 300 mW·cm<sup>-2</sup>; reaction temperature: 25 °C.

vibration of C-H in the AQ group.<sup>33,34</sup> Enhanced absorption peaks at 1278 cm<sup>-1</sup> (C-N stretching vibration) and 1676 cm<sup>-1</sup> (carbonyl C=O stretching vibration) further indicated the formation of an amide bond between AQ and CN-70%.<sup>36</sup> Additionally, Fig. S4 demonstrates that the triazine/heptazine ratio can be precisely tuned by adjusting the KCl composition in the molten salts. In the <sup>13</sup>C nuclear magnetic resonance (NMR) spectra (Fig. S5), the distinct signals observed at 163 ppm, 157 ppm, and 169 ppm for CN-70% and AQ/CN-70% are attributed to the CN<sub>2</sub>-NH<sub>x</sub> carbon atoms in the carbon nitride skeleton, C-N<sub>3</sub> carbon atoms, and the -C≡N carbon atoms, respectively.<sup>36</sup> For AQ/CN-70%, an additional set of new signals centered around 130 ppm emerged, which are ascribed to the aromatic C=C carbon atoms and carbonyl carbon atoms of the anthraquinone unit with slightly different chemical environments, confirming the successful incorporation of anthraquinone.<sup>37</sup> Furthermore, a new resonance appearing at approximately 180 ppm corresponds to the amide carbonyl carbon atom, indicating that the anthraquinone moiety is grafted onto the carbon nitride framework via amide linkage.<sup>38</sup> This signal exhibits a notable downfield shift compared to the carbonyl carbon of a typical primary amide (170-175 ppm), which likely originates from the strong intermolecular hydrogen bonding interactions.<sup>39</sup>

In the high-resolution XPS C 1s spectrum (Fig. 3b), characteristic peaks at 284.8, 286.1, and 288.1 eV correspond to C-C/C=C bonds, C-NH<sub>x</sub> (x=1 or 2) at the heptazine ring edges, and sp<sup>2</sup>-hybridized carbon (N-C=N) within the conjugated system, respectively. As shown in Fig. 1j and Table. S1, a notable increase in C-C/C=C content (from 22.7% in CN-70 to 27.8% in AQ/CN-70) was observed, which is attributed to

the successful introduction of anthraquinone units. The high-resolution N 1s spectra (Fig. S6) reveal peaks at 398.6, 400.2, 401.3, and 404.1 eV for all catalysts, assigned to sp<sup>2</sup>-hybridized nitrogen (C-N=C), tertiary nitrogen (N-(C)<sub>3</sub>), N-H<sub>x</sub> (x=1 or 2), and  $\pi$ - $\pi^*$  satellite transitions, respectively. As shown in Fig. S6a and Table. S2, comparison between AQ/CN-70% and CN-70%, the N-H<sub>x</sub> group content in AQ/CN-70% significantly decreased, which is attributed to the consumption of edge amino groups during the amidation reaction. Conversely, as shown in Fig. S6b, decreasing the KCl content led to a significant increase in the C-NH<sub>x</sub> proportion, suggesting that triazine-rich structures, which possess a higher density of edge amino groups, are more favourable for AQ modification. In contrast, CN-80% and AQ/CN-80% exhibited minimal changes in C-C/C=C content (Fig. S6c), indicating that the limited availability of edge amino groups in CN-80% hindered effective AQ coupling.

#### Photocatalytic H<sub>2</sub>O<sub>2</sub> production performance

The photocatalytic H<sub>2</sub>O<sub>2</sub> production of the prepared photocatalysts in pure water was assessed under visible light irradiation ( $\lambda \geq 420$  nm) in an open quartz tube under atmospheric conditions, with air serving as the O<sub>2</sub> source. As shown in Fig. 2a, pristine BCN exhibited a relatively low H<sub>2</sub>O<sub>2</sub> generation rate of 12.0  $\mu\text{mol g}^{-1} \text{h}^{-1}$ , whereas CN-70%, featuring a mixed triazine/heptazine units, achieved a higher rate of 35.9  $\mu\text{mol g}^{-1} \text{h}^{-1}$ . This enhancement suggests that the triazine/heptazine facilitates the separation of photogenerated charge carriers. Notably, after AQ modification, AQ/BCN and AQ/CN-70% demonstrated enhanced production rates of 25.6 and 165.3  $\mu\text{mol g}^{-1} \text{h}^{-1}$ , respectively. Meanwhile, the apparent quantum yield



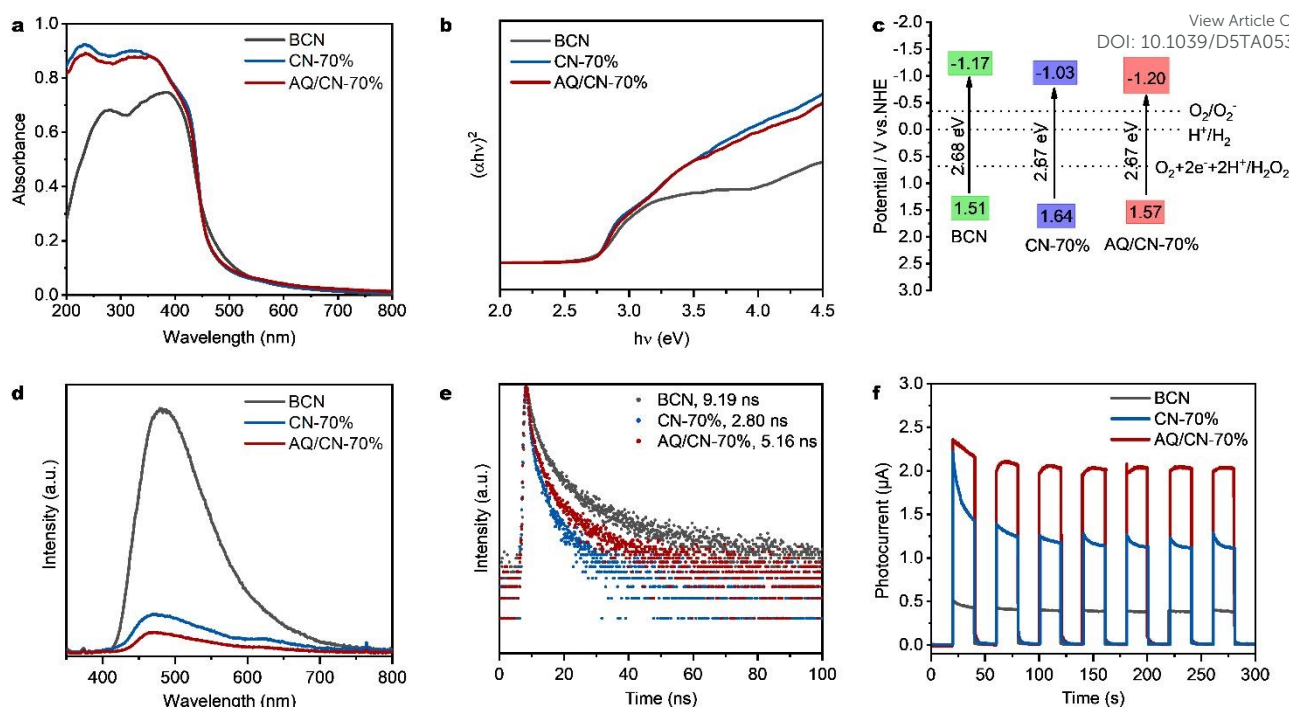


**Fig. 3** (a) UV-Vis DRS and (b) Tauc Plot of BCN, CN-70% and AQ/CN-70%, (c) Band structure alignments of BCN, CN-70% and AQ/CN-70%, (d) Steady-state PL spectra, (e) Time-resolved transient PL spectra and (f) Transient photocurrent responses of BCN, CN-70%, and AQ/CN-70%.

(AQY) of AQ/CN-70% was also measured and the results were presented in Table S3. Under 420 nm irradiation, the AQY reached 2.48%, suggesting that AQ/CN-70% exhibits high light-to-chemical energy conversion efficiency. Given that triazine units offer more modification sites, it is essential to further investigate the influence of triazine content on  $\text{H}_2\text{O}_2$  production. As depicted in Fig. 2b, the  $\text{H}_2\text{O}_2$  production rate gradually decreased as the KCl ratio decreased from 90% to 60%, which can be attributed to the superior photocatalytic  $\text{H}_2\text{O}_2$  generation performance of heptazine units compared to triazine units.<sup>40</sup> After AQ modification, all AQ/CN-x% samples exhibited enhanced catalytic activity to varying degrees, with AQ/CN-70% showing the highest  $\text{H}_2\text{O}_2$  production rate (Fig. 2c). This can be explained by the fact that in CN-90%, the limited amino groups result in insufficient AQ modification. Conversely, when the triazine content is too high (CN-60%), the charge separation efficiency and  $\text{O}_2$  reduction capability is suppressed. Thus, AQ/CN-70% with balanced triazine/heptazine ratio demonstrated optimal photocatalytic activity.

Photocatalytic performance tests under different atmospheres revealed the following order of  $\text{H}_2\text{O}_2$  production:  $\text{O}_2 > \text{Air} > \text{Ar}$  (Fig. 2d), indicating that  $\text{O}_2$  is an indispensable reactant for  $\text{H}_2\text{O}_2$  synthesis. With prolonged illumination time, the cumulative  $\text{H}_2\text{O}_2$  production continuously increased (Fig. 2e), demonstrating that the catalyst maintains good catalytic efficiency over extended periods. Furthermore, cycling stability tests showed only a slight decrease in photoactivity in two consecutive runs (Fig. 2f), which might be attributed to the protonation of key active sites leading to reduced catalytic performance.<sup>41</sup> Notably, the photoactivity maintained stable in subsequent cycles, confirming that the AQ units remained structurally intact throughout the catalytic process. To corroborate

this observation, we examined the structural evolution of the material before and after photocatalytic reactions (Fig. S7). The XRD patterns (Fig. S7a) revealed no significant alteration in the crystalline structure. Similarly, the FTIR spectra (Fig. S7b) confirmed the persistence of characteristic peaks associated with the AQ motifs. However, the intensities of the two peaks located at  $1178\text{ cm}^{-1}$  and  $998\text{ cm}^{-1}$ , which are assigned to the  $\text{K}^+$ -coordinated  $\text{C}=\text{N}=\text{C}$  bonds,<sup>42-44</sup> were significantly reduced. This indicates that the performance degradation is indeed caused by protonation. Electron microscopy revealed that the molten salt synthesis induced morphological changes, potentially influencing specific surface area and influencing consequently photocatalytic performance. Nitrogen adsorption-desorption measurements (Figs. S8a-e) revealed that all samples exhibit similar pore size distributions. However, CN-70% and AQ/CN-70% exhibited comparable specific surface areas ( $75.4\text{ m}^2\text{ g}^{-1}$  and  $88.0\text{ m}^2\text{ g}^{-1}$ , respectively), both of which are significantly larger than that of pristine BCN ( $36.7\text{ m}^2\text{ g}^{-1}$ ). To disentangle surface area effects from intrinsic activity, we normalized the catalytic performance (Fig. S9). The results demonstrate that the substantial activity enhancement stems primarily from improved intrinsic activity due to AQ functionalization, rather than merely increased surface area.

#### Mechanism of photocatalytic hydrogen peroxide production

To elucidate the intrinsic mechanism underlying the enhanced photocatalytic performance, we comprehensively characterized the light absorption capability and band structure of the photocatalysts. UV-Vis diffuse reflectance spectroscopy (UV-Vis DRS) exhibited a slight red shift in the absorption edge and enhanced absorption intensity in the  $\lambda < 450\text{ nm}$  region for CN-70% (Fig. 3a). After Kubelka-Munk transformation of the UV-Vis absorption spectra, the optical bandgap energies of BCN, CN-70% and AQ/CN-70% were determined



## PAPER

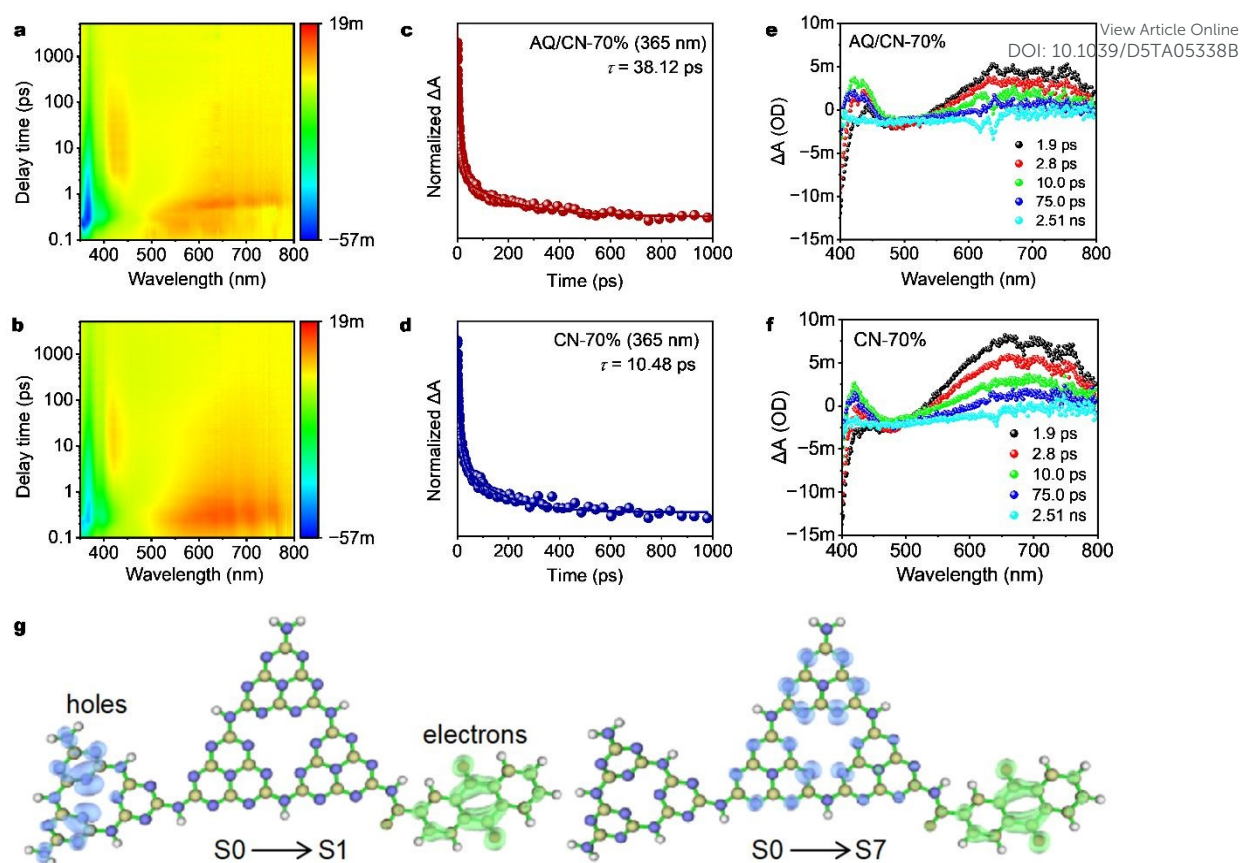


**Fig. 4** 2D mapping TA spectra of (a) AQ/CN-70% and (b) CN-70%, TA spectra signals on the fs-ns timescales of (c) AQ/CN-70% and (d) CN-70%, decay kinetic curves of (e) AQ/CN-70% and (f) CN-70%, (g) The excited state information in AQ/CN-70% from DFT calculations.

to be 2.68 eV, 2.67 eV and 2.67 eV, respectively (Fig. 3b). Therefore, AQ modification did not alter the bandgap structure of CN-70%, indicating that the improvement in photocatalytic activity primarily originated from the AQ moiety. Fig. S10 presents the XPS valence band analysis results, showing that the valence band positions of BCN, CN-70%, and AQ/CN-70% relative to the normal hydrogen electrode (NHE) were 1.51 V, 1.64 V and 1.57 V, respectively. Based on the fundamental relationship  $E_g = E_{VB} - E_{CB}$ , the corresponding conduction band positions were calculated to be -1.17 V (BCN), -1.03 V (CN-70%) and -1.20 V (AQ/CN-70%), respectively. Fig. 3c illustrates the band structure diagram of the three photocatalysts, demonstrating all of them are suitable for driving oxygen reduction to generate  $H_2O_2$ .<sup>45</sup>

We then disclosed charge carrier separation and transfer dynamics through steady-state photoluminescence (PL) spectroscopy, time-resolved photoluminescence (TRPL) spectroscopy and transient photocurrent measurements. PL spectra revealed a significant reduction in emission intensity for CN-70% compared to pristine BCN (Fig. 3d), indicating that the triazine rich g- $C_3N_4$  markedly enhanced charge separation efficiency. Notably, after AQ modification, the PL intensity of AQ/CN-70% further decreased, demonstrating that AQ functionalization could further promote the separation of photogenerated charges.<sup>46</sup> This finding was corroborated by TRPL measurements. As shown in Fig. 3e and Fig. S11, significantly shorter

fluorescence lifetimes were observed for AQ/CN-70% and CN-70%, suggesting enhanced exciton dissociation into free charge carriers. Interestingly, AQ/CN-70% exhibited a slightly prolonged fluorescence lifetime compared to CN-70%, which can be attributed to the electron-withdrawing nature of AQ units suppressed electron-hole recombination and extending charge carrier lifetimes.<sup>47</sup> Furthermore, transient photocurrent responses mirrored the photocatalytic activity trend (AQ/CN-70% > CN-70% > BCN). AQ/CN-70% generated the highest photocurrent density (Fig. 3f), directly evidencing that AQ modification effectively improved the separation efficiency of photogenerated charges.

To further investigate the dynamics of photoexcited states, we conducted femtosecond-transient absorption spectroscopy (fs-TAS) analysis. As shown in Figs. 4a and 4b, the negative absorption peak at 350 nm corresponds to the ground-state bleaching (GSB) signal, originating from the pump-light excitation of the photocatalyst. All samples exhibited strong GSB signals, which subsequently decayed rapidly due to electron-hole recombination.<sup>48</sup> The GSB signal intensity of AQ/CN-70% was significantly higher than that of CN-70%, indicating that AQ modification effectively increased the population of shallowly trapped electrons. Compared to CN-70%, AQ/CN-70% exhibited a notably prolonged GSB signal lifetime (Figs. 4c and 4d), demonstrating that the introduction of AQ units successfully suppressed electron-hole recombination.<sup>45</sup> The broad positive





absorption feature observed in the 500-800 nm range represents the excited-state absorption (ESA) of shallowly trapped electrons.<sup>49</sup> The emergence of this positive signal reflects the enrichment of shallowly trapped electrons. (Figs. S12a and S12c) show that the lifetime of the excited-state electrons in AQ/CN-70% was significantly shortened, suggesting rapid transfer of excited-state electrons.<sup>50</sup> The characteristic transient absorption peaks in the 400 - 450 nm range originate from high-energy electronic transitions associated with Auger recombination of shallowly trapped charge carriers.<sup>51,52</sup> Kinetic analysis (Figs. 4e, 4f and S13a,b) revealed that these narrow positive peaks appeared synchronously with the decay of the broad ESA signal (500 - 800 nm), exhibiting a characteristic lifetime of 300-400 ps (Figs. S12b and S12d), consistent with the emergence of high-energy Auger electrons. Notably, AQ/CN-70% not only retained the characteristic transitions

observed in CN-70% at 400 - 450 nm but also exhibited a new peak at longer wavelengths. The appearance of this new peak suggests that the introduction of AQ units in AQ/CN-70% created a new energy level, which effectively captured high-energy electrons. This appearance of the new peak suggests that the introduction of AQ units in AQ/CN-70% created a new energy level, which effectively captured high-energy electrons generated *via* the Auger recombination process. DFT calculations (Figs. 4g and S14) further confirmed that the AQ group acts as an effective electron-withdrawing centre. Based on experimental and theoretical results, it was further demonstrated that the AQ units significantly enhanced charge separation due to their electron-withdrawing nature. Therefore, the AQ units not only promoted enhanced excited-state charge transfer but also suppressed electron-hole recombination, endowing AQ/CN-70% with exceptional photocatalytic performance.

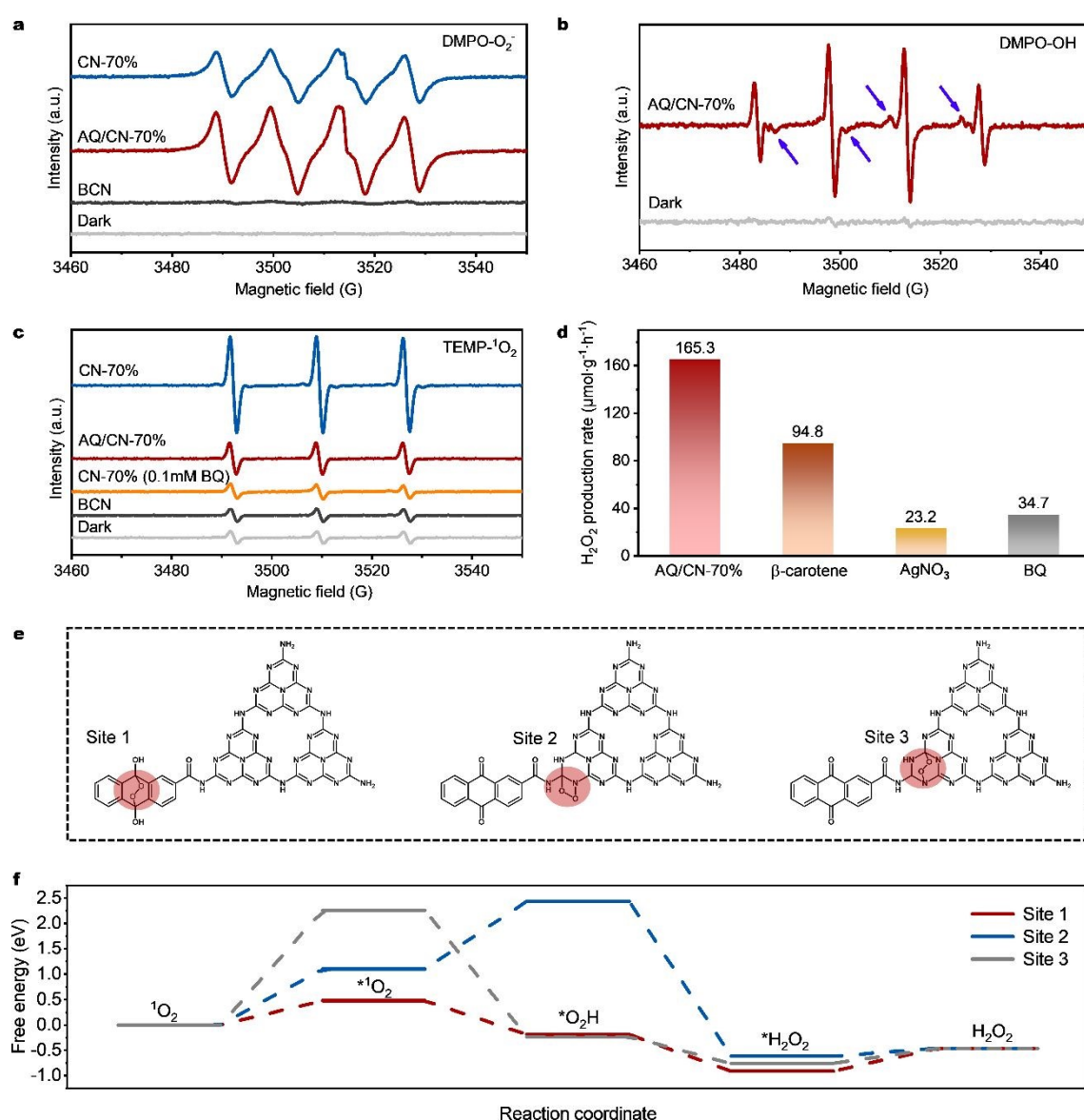


**Fig. 5** (a)  $\cdot\text{O}_2^-$ , (b)  $\cdot\text{OH}$  and (c)  $^1\text{O}_2$  radical adduct signals in EPR spectra of BCN, CN-70%, AQ/CN-70% and CN-70% with the addition of BQ, (d)  $\text{H}_2\text{O}_2$  production rates of AQ/CN-70% with different radical scavengers, (e) Schematic illustration of potential  $^1\text{O}_2$  reaction sites, (f) Free energy diagrams for  $\text{H}_2\text{O}_2$  formation pathways at distinct reaction sites on AQ/CN-70%.





## PAPER

By performing EPR during visible-light irradiation, we deciphered the radical-mediated reaction mechanism governing photocatalytic  $\text{H}_2\text{O}_2$  production on the AQ/CN-70% catalyst. As shown in Fig. 5a, EPR measurements using 5,5-Dimethyl-1-Pyrroline N-Oxide (DMPO) as a radical trapping agent in methanol solution detected no signal for AQ/CN-70% in the dark. Upon illumination, a characteristic  $\cdot\text{O}_2^-$  signal appeared with significantly greater intensity than that of CN-70%, indicating that AQ modification enhanced charge separation and consequently improved the efficiency of  $\text{O}_2$  reduction to  $\cdot\text{O}_2^-$ . Fig. 5b reveals the characteristic  $\cdot\text{OH}$  signal peaks of AQ/CN-70% in deionized water using DMPO as a radical trapping agent during EPR testing, along with a quartet signal (blue arrow) attributed to  $\cdot\text{OOH}$  radicals, suggesting a two-step single-electron oxygen reduction pathway for  $\text{H}_2\text{O}_2$  production. Fig. 5c presents the EPR spectra of 2,2,6,6-tetramethyl-4-piperidone (TEMP)-trapped singlet oxygen ( $^1\text{O}_2$ ). CN-70% exhibited the strongest  $^1\text{O}_2$  signal. When the superoxide radical ( $\cdot\text{O}_2^-$ ) was scavenged by the quencher *p*-benzoquinone (BQ), the  $^1\text{O}_2$  signal in CN-70% significantly weakened, confirming that the oxidation of  $\cdot\text{O}_2^-$  by holes is the primary pathway for  $^1\text{O}_2$  generation. Therefore, the consumption of the intermediate  $\cdot\text{O}_2^-$  for  $^1\text{O}_2$  formation competes with  $\text{H}_2\text{O}_2$  production, adversely affecting photocatalytic performance. Fig. S15 reveals identical behaviour in AQ/CN-70%. Surprisingly, the  $^1\text{O}_2$  signal also sharply decreased after AQ modification (Fig. 5c). Given that the  $\cdot\text{O}_2^-$  signal in AQ/CN-70% was enhanced under illumination, it is reasonable to conclude that the weakened  $^1\text{O}_2$  signal primarily results from the trapping and conversion of  $^1\text{O}_2$  by AQ units. To investigate the contributions of different reactive species to  $\text{H}_2\text{O}_2$  generation, quenching experiments were conducted using specific scavengers: carotene (for  $^1\text{O}_2$ ),  $\text{AgNO}_3$  (for  $\text{e}^-$ ) and BQ (for  $\cdot\text{O}_2^-$ ). As shown in Fig. 5d, the addition of  $\beta$ -carotene reduced the  $\text{H}_2\text{O}_2$  yield from 165.3 to 94.8  $\mu\text{mol g}^{-1} \text{h}^{-1}$ , indicating that  $^1\text{O}_2$  contributes partially to  $\text{H}_2\text{O}_2$  production. When  $\text{AgNO}_3$  ( $\text{e}^-$  scavenger) and BQ ( $\cdot\text{O}_2^-$  scavenger) were introduced, the  $\text{H}_2\text{O}_2$  yield dropped drastically, confirming that electrons and  $\cdot\text{O}_2^-$  remain the key reactive species. Based on the RDE measurements, the electron transfer number for AQ/CN-70% during the reaction was determined to be 1.89 (Fig. S16), indicating that AQ/CN-70% indeed produces hydrogen peroxide via a two-electron oxygen reduction reaction (ORR) pathway.

DFT calculations were further performed to evaluate the free energy of different  $^1\text{O}_2$  reaction sites on AQ/CN-70%. As shown in Figs. 5e, f and S17, the results revealed that, compared to the reaction sites in pristine carbon nitride (Site 2 and Site 3), the AQ site (Site 1) exhibited a significantly more favourable Gibbs free energy change ( $\Delta\text{G}$ ) for the formation of  $\cdot^1\text{O}_2$  and  $\cdot\text{OOH}$  intermediates. This indicates that the AQ site is more efficient in reducing  $^1\text{O}_2$  to  $\text{H}_2\text{O}_2$ . These findings further confirm that the AQ unit serves as the active site for converting  $^1\text{O}_2$  into  $\text{H}_2\text{O}_2$ . Therefore, AQ modification not only enhances charge separation but, more importantly, transforms the generated  $^1\text{O}_2$  into the target product  $\text{H}_2\text{O}_2$ . This strategy ingeniously converts an otherwise competing side reaction into a favourable pathway for  $\text{H}_2\text{O}_2$  production, fundamentally improving the efficiency of photocatalytic  $\text{H}_2\text{O}_2$  synthesis.

Integrated experimental and theoretical evidence confirms the charge transfer dynamics in AQ/CN-70% (Fig. 6), characterized by hole accumulation at triazine units and electron localization on anthraquinone moieties. This spatial separation creates donor-acceptor (D-A) configurations, significantly enhancing charge separation efficiency and thereby boosting photocatalytic performance. EPR analysis reveals dual  $\text{H}_2\text{O}_2$  production pathways: (1) conventional  $\text{O}_2 \rightarrow \cdot\text{O}_2^- \rightarrow \text{H}_2\text{O}_2$  reduction, and (2) a synergistic AQ/ $\text{H}_2\text{AQ}$  cycle that converts detrimental  $^1\text{O}_2$  into  $\text{H}_2\text{O}_2$  through: (i)  $\text{AQ} + 2\text{e}^- + 2\text{H}^+ \rightarrow \text{H}_2\text{AQ}$  (proton-coupled electron transfer), (ii)  $\text{H}_2\text{AQ} + ^1\text{O}_2 \rightarrow \text{H}_2\text{O}_2 + \text{AQ}$  (singlet oxygen scavenging). This dual-reduction mechanism circumvents kinetic limitations from competitive  $\cdot\text{O}_2^-$  oxidation, substantially elevating  $\text{H}_2\text{O}_2$  production yields.

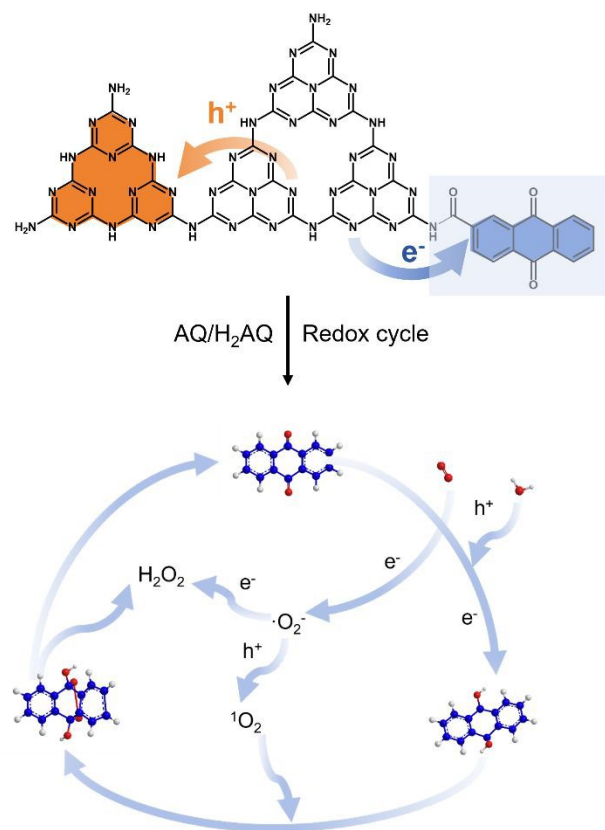


Fig. 6 Charge transfer and AQ/ $\text{H}_2\text{AQ}$  redox cycle mechanism for photocatalytic  $\text{H}_2\text{O}_2$  synthesis on AQ/CN- $x\%$  catalyst.

## Conclusions

In conclusion, the AQ/CN-70% photocatalyst was successfully prepared through molten salt-assisted calcination followed by amide condensation to anchor AQ units. The triazine rich  $\text{g-C}_3\text{N}_4$  framework provided abundant modification sites. After AQ functionalization, the catalyst demonstrated significantly enhanced visible-light-driven  $\text{H}_2\text{O}_2$  production in pure water, achieving a remarkable yield of 165.3  $\mu\text{mol g}^{-1} \text{h}^{-1}$ , which is 13.8 times higher than that of pristine  $\text{g-C}_3\text{N}_4$ . fs-TAS combined with theoretical calculations revealed that the AQ unit acts as an electron-trapping centre, substantially accelerating excited-state electron transfer while prolonging electron relaxation time. EPR spectroscopy and radical trapping experiments further confirmed that the introduction of AQ units effectively suppressed



singlet oxygen ( $^1\text{O}_2$ ) accumulation and instead facilitated its participation as an intermediate in  $\text{H}_2\text{O}_2$  synthesis. This work presents a novel strategy for converting the competitive  $^1\text{O}_2$  generation pathway into  $\text{H}_2\text{O}_2$  production by AQ modification, offering valuable insights into simultaneously improving charge separation efficiency and enhancing  $\text{H}_2\text{O}_2$  synthesis performance.

## Author Contributions

C. Zhou, G. Chen and X. Meng conceived the idea and designed the experiments. T. Zhang supervised the project. J. Li, L. Wang, H. Zhang and Q. Chen carried out the experiments and characterizations. J. Li, C. Zhou, G. Chen and X. Meng wrote the manuscript. All the authors discussed the results and commented on the manuscript.

## Conflicts of interest

There are no conflicts to declare.

## Acknowledgements

The authors are grateful for financial support from the National Key Projects for Fundamental Research and Development of China (2023YFA1507201, 2021YFA1500803), the National Natural Science Foundation of China (22421005, 52120105002, 52432006, 22279150, 22479151 and 22088102), the CAS Project for Young Scientists in Basic Research (YSBR-004), the international partnership program of Chinese Academy of Sciences (174GJHZ2024054MI), Liaoning Binhai Laboratory (LBLD-2024-06). G. Chen thanks the fundings from the National Key R&D Program of China (2024YFA1510700) and Science Fund Program for Excellent Young Scientists (Overseas) of the National Natural Science Foundation of China.

## Notes and references

- X. Yu, Y. Hu, C. Shao, W. Huang and Y. Li. *Mater. Today*, 2023, **71**, 152-173.
- Z. Li, S. Liu, D. Zhang, B. Cai, Y. Liang, M. Wu, Y. Liao and X. Zhao, *Angew. Chem., Int. Ed.*, 2024, **63**(23), 202404563.
- Y. Sun, L. Han and P. Strasser. *Chem. Soc. Rev.*, 2020, **49**, 6605-6631.
- Alam, A, Kumbhakar. B, Chakraborty. A, Mishra. B, Ghosh. S, Thomas. A, Pachfule. P. *ACS Mater Lett.*, 2024, **6**, 2007-2049.
- Ajay, Dimple, Verma. P, Yamashita. H, *Chem Catal.*, 2024, **4**, 2667-2693.
- Y. Zhao, Y. Kondo, Y. Kuwahara, K. Mori, H. Yamashita. *Appl. Catal., B.*, 2024, **351**, 123945.
- S.-S Zhu, Z. Zhang, Z. Li, H. Yue., X. Liu. *Chem Catal.*, 2024, **4**, 2667-2707.
- S. Cai, W. Wu, T. Liu, Z. Li, H. Chang, P. R. Galligan, S. Iida, X. Li, F. Rehman, K. Amine, W. A. Goddard, Z. Luo, *J. Mater. Chem. A* 2023 **11**, 7513-7525.
- H. Huang, W. Xie, Q. Wan, L. Mao, D. Hu, H. Sun, X. Zhang and Y. Wei. *Adv. Sci.*, 2021, **9**, 2104101.
- Z. Teng, H. Yang, Q. Zhang, W. Cai, Y.-R. Lu, K. Kato, Z. Zhang, J. Ding, H. Sun, S. Liu, C. Wang, P. Chen, A. Yamakata, D. S. Chan, C. Su, T. Ohno and B. Liu. *Nat. Chem.*, 2024, **16**, 1250-1260.
- X. Zeng, T. Wang, Z. Wang, M. Tebyetekerwa, Y. Liu, Z. Liu, G. Wang, A. A. Wibowo, G. Pierens, Q. Gu and X. Zhang. *ACS Catal.*, 2024, **14**, 9955-9968.
- Y. Shen, Y. Yao, C. Zhu, J. Wu, L. Chen, Q. Fang and S. Song. *Chem. Eng. J.*, 2023, **475**, 146383.
- S. Wen, L. Z. Y. Liu, B. Wang, K. Zhang, S. Tang and Y. Li. *J. Colloid Interface Sci.*, 2024, **656**, 80-92.
- P. Li, Y. Zhang, H. Liu, Y. Fang, S. Li, X. Hu and Q. Chen. *J. Colloid Interface Sci.*, 2025, **682**, 725-737.
- Q. Zhang, B. Wang, H. Miao, J. Fan, T. Sun and E. Liu. *Chem. Eng. J.*, 2024, **482**, 148844.
- J. Cheng, S. Wan and S. Cao, *Angew. Chem., Int. Ed.*, 2023, **62**, e202310476.
- Z. Li, Q. Yang, H. Zhang, F. Zheng, Y. Wang and J. Sun. *Sustain. Energy Fuels*, 2024, **8**, 1338-1345.
- H. Kim, C. Yeoseon, H. Shu, Choi. Wonyong, Jae-Hong Kim. *Appl. Catal., B*, 2018, **229**, 121-129.
- P. Pracht., S. Grimme, C. Bannwarth, F. Bohle., S. Ehlert, G. Feldmann, J. Gorges, M. Müller, T. Neudecker, C. Plett, S. Spicher, P. Steinbach, P. A. Wesolowski, F. Zeller. *J. Chem. Phys.*, 2024, **160**, 114110.
- C. Bannwarth, S. Ehlert and S. Grimme. *J. Chem. Theory Comput.*, 2019, **15**, 1652-1671.
- A. D. Becke. *J. Chem. Phys.*, 1993, **98**, 5648-5652.
- C. Lee, W. Yang and R. G. Parr. *Phys. Rev. B*, 1988, **37**, 785-789.
- P. J. Stephens, F. J. Devlin, C. F. Chabalowski, M. J. Frisch. *J. Phys. Chem.*, 1994, **98**, 11623-11627.
- T. H. Dunning. *J. Chem. Phys.*, 1970, **53**, 2823-2833.
- P. C. Hariharan and J. A. Pople. *Theor. Chim. Acta*, 1973, **28**, 213-222.
- W. J. Hehre, R. Ditchfield and J. A. Pople. *J. Chem. Phys.*, 1972, **56**, 2257-2261.
- S. Grimme, Hansen, A, Brandenburg. J. G, Bannwarth. C. *Chem. Rev.*, 2016, **116**, 5105-5154.
- S. Grimme, S. Ehrlich and L. Goerigk. *J. Comput. Chem.*, 2011, **32**, 1456-1465.
- T. Lu and F. Chen. *J. Comput. Chem.*, 2012, **33**, 580-592.
- F. Li, X. Yue and Y. Liao. *Nat. Commun.*, 2023, **14**, 3901.
- R Guan, A Shi, X Zhang, B Wang, Y Li, and X Niu. *ACS Catalysis*. 2024, **14** (24), 18580-18589
- L. Mao, B. Zhai, J. Shi, X. Kang, B. Lu, Y. Liu, C. Cheng, H. Jin, E. Lichtfouse and L. Guo. *ACS. Nano*, 2024, **18**, 13939-13949.
- Q. Zhang, K. Gu, C. Dong, C. Xue, H. Che, K. Zhang and Y. Ao. *Angew. Chem. Int. Ed.*, 2025, **64**, e202417591.
- S. Martha, A. Nashim and K. M. Parida. *J. Mater. Chem. A*, 2013, **1**, 7816-7824.
- I. Krivtsov, A. Vazirani, D. Mitoraj, M. M. Elnagar and R. Beranek. *J. Mater. Chem. A*, 2023, **11**, 2314-2323.
- Q. Zhang, J. Chen, H. Che, B. Liu, Y. Ao, *Small*, 2023, **9**, 2302510.
- Y. Huang, D. Li, Z. Fang, R. Chen, B. Luo, W. Shi, *Appl. Catal. B*, 2019, **254**, 128-134.
- Z. Zhou, T. Deng, M. Tao, L. Yang, M. Wu, *Biomaterials*, 2023, **299**, 122141.
- D.L Vanderhart, William L Earl, A.N Garroway, *J. Magn. Reson.*, 1981, **44**, 361-401.
- C. Chu, Q. Zhu and Z. Pan, *Proc. Natl. Acad. Sci.*, 2020, **117**, 6376-6382.
- P. Zhang, J. Li, W. Sun, C. Zhou and X. Meng. *Mater. Lett.*, 2025, **382**, 137954.



## PAPER

- 42 B. Zhai, H. Li, G. Gao, Y. Wang, P. Niu, S. Wang and L. Li. *Adv. Funct. Mater.*, 2022, **32**, 2207375.
- 43 B. Zhai, J. Zeng, Y. Wang, P. Niu, S. Wang and L. Li. *Appl. Catal. B: Environ. Energy*, 2024, **359**, 124496
- 44 C. Liu, Y. Zhu, S. Di, J. He, P. Niu, A. Kelarakis, M. Krysmann, S. Wang and L. Li. *Electron* 2024, **2**, e29.
- 45 Y. Ham, K. Maeda, D. Cha, K. Takanabe and K. Domen. *Chem. Asian J.*, 2013, **8**, 218-224.
- 46 J. Ma, R. Long, D. Liu, J. Low, Y. Xiong. *Small Struct.*, 2022, **3**, 2100147.
- 47 C. Li, Y. Du, D. Wang, S. Yin, W. Tu, Z. Chen, M. Kraft, G. Chen, R. Xu. *Adv. Funct. Mater.*, 2017, **27**, 1604328.
- 48 Y. Mou, X. Wu, C. Qin, J. Chen, Y. Zhao, L. Jiang, C. Zhang, X. Yuan, E. H. X. Ang, H. Wang. *Angew. Chem. Int. Ed.*, 2023, **62**, e202309480.
- 49 M. Qian, X. L. Wu, M. Lu, L. Huang, W. Li, H. Lin, J. Chen, S. Wang, X. Duan. *Adv. Funct. Mater.*, 2023, **33**, 2208688.
- 50 G. Zhang, Y. Xu, M. Rauf, J. Zhu, Y. Li, C. He, X. Ren, P. Zhang, H. Mi. *Adv. Sci.* 2022, **9**, 2201677.
- 51 R. Godin, Y. Wang, M. A. Zwiijnenburg, J. Tang, J. R. Durrant. *J. Am. Chem. Soc.* 2017, **139**, 5216-5224.
- 52 F. Gesuele, M. Y. Sfeir, W. K. Koh, C. B. Murray, T. F. Heinz, C. W. Wong. *Nano. Lett.*, 2012, **12**, 2658-2664.

View Article Online  
DOI: 10.1039/D5TA05338B





[View Article Online](#)

DOI: 10.1039/D5TA05338B

The data supporting this article are included in the Electronic Supplementary Information (ESI).

